Fixed Wing UAV Path Following in Wind With Input Constraints

Randal W. Beard, Jeff Ferrin, and Jeffrey Humpherys

***Abstract*— This paper considers the problem of fixed wing unmanned air vehicles following straight lines and orbits. To account for ambient winds, we use a path following approach as opposed to trajectory tracking. The unique feature of this paper is that we explicitly account for roll and flight path angle constraints. The guidance laws are derived using the theory of nested saturations, and explicit flight conditions are derived that guarantee convergence to the path. The method is validated by simulation and flight tests.**

***Index Terms*— Aircraft Navigation, motion planning, nonlinear control systems, unmanned systems.**

I. Introduction

MANY applications of small and miniature unmanned aeriel vehicles (UAVs) require that the vehicle traverse an inertially defined path. For example, the UAV may be required to survey a series of geographic features where the objective is to record images of the features. In these applications, it is important that the UAV be on the path, but the time parameterization of the path may not be critical. One approach to this problem is to impose a time parameterization of the path and to pose the associated trajectory tracking problem. However, this approach is not well suited to small and miniature fixed wing UAVs since the ambient wind can be a significant percentage of the airspeed of the vehicle.

Fixed wing vehicles are typically designed to fly at a particular airspeed to maximize fuel efficiency. However, flying at a constant airspeed is not compatible with trajectory tracking in wind. For example, consider the case where the desired path is a circular orbit and there is a strong ambient wind. If the time parameterization calls for a constant speed with respect to the ground, then airspeed will need to increase significantly when the vehicle is heading into the wind, and will need to decrease significantly when the vehicle is heading downwind. Not only do these large variations in the airspeed reduce the fuel efficiency, they can also cause the vehicle to stall in downwind conditions.

An alternative to trajectory tracking is path following where the vehicle attempts to regulate its distance from the geometrically defined path, as opposed to regulate the error from a time varying trajectory.

The path-following approach is studied in [1] and [2], where performance limits for reference-tracking and path-following controllers are investigated and the difference between them is highlighted. It is shown that there is not a fundamental performance limitation for path following for systems with unstable zero dynamics as there is for reference tracking.

Building on the work presented in [3] on maneuver modified trajectory tracking, [4] develops an approach that combines the features of trajectory tracking and path following for marine vehicles. Similarly, [5] develops an output maneuver method composed of two tasks: forcing the output to converge to the desired path and then satisfying a desired speed assignment along the path. The method is demonstrated using a marine vessel simulation. Reference [6] presents a path following method for UAVs that provides a constant line of sight between the UAV and an observation target.

A path following strategy for UAVs that is becoming increasingly popular is the notion of a vector field [7]–[9]. The basic idea is to calculate a desired heading based on the distance from the path. A nice extension of [8] is given in [10], which derives general stability conditions for vector-field-based methods. The focus in [10] is circular orbits. An extension to general paths that are diffeomorphic to a circle is reported in [11], including 3-D paths. However, the vehicle model used in [10] and [11] is a single integrator and does not explicitly consider the nonholonomic kinematic model of the vehicle or input constraints. In [12], the vector field concept is extended to velocity following in n-dimensional spaces. The path to be followed is specified as the intersection of the level set of $n - 1$ scalar functions. The control law is composed of a stabilizing term that renders the path attractive, and a circulation term that forces the system to progress along the path. Similar to [10] and [11], the formulation in [12] does not explicitly consider nonholonomic kinematics or input constraints.

Another related method is reported in [13], which uses adaptive backstepping to estimate the direction of the wind and to track a straight-line path. The techniques in [13] are only applied to 2-D vehicles following a straight-line path, and assume skid-to-turn dynamics without actuator constraints.

In [14], a pure pursuit missile guidance law is adapted and used for UAV path following. The basic idea is to command the UAV to follow a reference point on the desired path that is a fixed distance in front of the vehicle. Similar to the missile guidance literature, an acceleration command is generated to align the velocity vector with the line-of-sight vector to the

Manuscript received July 30, 2013; revised October 23, 2013; accepted January 23, 2014. Manuscript received in final form January 28, 2014. Recommended by Associate Editor M. Mattei.

R. W. Beard is with the Electrical and Computer Engineering Department, Brigham Young University, Provo, UT 84602 USA (e-mail: beard@byu.edu).

J. Ferrin is with MAGICC Lab, Brigham Young University, Provo, UT 84602 USA (e-mail: jeff ferrin@hotmail.com).

J. Humphreys is with the Mathematics Department, Brigham Young University, Provo, UT 84602 USA (e-mail: jeffh@math.byu.edu).

Color versions of one or more of the figures in this paper are available online at http://ieeexplore.ieee.org.

Digital Object Identifier 10.1109/TCST.2014.2303787

target point. The full nonlinear guidance strategy is analyzed using set invariance and Lyapunov theory. There is also an analysis when the acceleration command is saturated and it is shown that the region of stability decreases. The method is demonstrated in flight with two vehicles in a leader follower configuration. While the acceleration command is explicitly saturated, for the control strategy to be implemented on the autopilot, the acceleration constraints need to be converted to roll angle, flight path, and airspeed constraints. The analytic relationship between the acceleration and roll angle, flight angle, and airspeed depends on aerodynamic models of the aircraft and may not be available, especially for small UAVs. As an alternative, in this paper, we develop a path following strategy that directly constrains the roll and the flight path angles, and where the airspeed is fixed at a constant value.

The main analytical tool that we use in this paper is the theory of nested saturation, which was introduced in [15] to control a cascade of integrators with input and state constraints. The technique was extended in [16] to systems with nonlinearities in the input channels, and was applied to the control of a planar vertical take-off and landing aircraft with bounded thrust and torque. In [17], nonlinear control strategies based on nested saturation are developed for the roll and pitch axis of a quadrotor, and experimental results are reported. The strategy that we develop in this paper is motivated by the results reported in [16] and [17], and the need to constrain the roll and the flight path angles for small scale UAVs. However, the equations of motion of fixed wing UAVs differs from the systems considered in [16] and [17] in the sense that rather than working with second-order dynamic systems, we look at controlling the kinematic equations of motion where there are nonlinearities between the first and second integrators of the system. In particular, the theory of nested saturations is applied to an extended Dubins airplane model [18]. It turns out that this extension is not trivial.

The objective of this paper is to develop path following strategies that explicitly account for roll and flight path angle constraints. Previous work has primarily addressed constant altitude maneuvers whereas in this paper we also consider climb maneuvers. This paper focuses on following straight-line segments and circular orbits. Our motivation for limiting the focus to these maneuvers is based on the approach described in [7] where straight-line and circular orbits are concatenated to create more complicated paths.

The specific contributions of this paper are as follows. First, roll and flight path angle constraints, which are absolutely necessary for small UAV flight, are explicitly satisfied using the theory of nested saturation. Second, the nested saturation technique is extended to the problem of path following, which is a guidance task as opposed to previous work that considers dynamic stabilization. This is a nontrivial extension since we are required to work with kinematic expressions instead of dynamic equations of motion. The kinematic expressions contain nonlinearities between the integrators and therefore pose additional challenges to the use of nested saturation. Third, we explicitly account for wind and derive conditions on the magnitude of the wind such that path following is still guaranteed in the presence of roll and flight path angle constraints. Fourth, the control strategy for orbit following is complicated by the fact that the nested saturation controller is not guaranteed to converge in a region around the center of the orbit. To account for this, we have introduced a switching strategy and have derived stability conditions that show that asymptotic path following is achieved from any initial configuration (subjected to wind constraints). Finally, we have implemented the proposed guidance strategies on a small UAV and demonstrated their effectiveness in flight. A preliminary version of this paper appeared in [19]. However, [19] did not address the presence of wind, did not include the longitudinal controller, did not include analytical proofs for the results, and did not include flight results, all of which appear in this paper.

The remainder of this paper is organized as follows. The kinematic equations of motion for a fixed wing UAV are listed in Section II. A guidance strategy for straight-line path following is derived in Section III together with six-degrees-of-freedom (DOF) simulation results that illustrate the effect of the parameters used in the guidance law. A guidance strategy for orbit following, as well as similar simulation studies, is given in Section IV. Flight test results using a small Zagi style model aircraft are given in Section V, and some concluding remarks are given in Section VI.

II. Equations of Motion

If p_n and p_e are the inertial north and east position of the vehicle, and h is the altitude, then the kinematic model of a fixed wing unmanned air vehicle in wind can be given by [7]

$$\dot{p}_n = V\cos\psi\cos\gamma + w_n \tag{1}$$

$$\dot{p}_e = V\sin\psi\cos\gamma + w_e \tag{2}$$

$$\dot{h} = V\sin\gamma + w_h \tag{3}$$

where V is the airspeed, ψ is the heading angle measured from north, γ is the air mass referenced flight path angle, and w_n, w_e, and w_h are the north, east, and altitude components of the wind. We will assume that the wind vector is constant. We will assume throughout this paper the existence of a low level autopilot that maintains a constant airspeed. We also assume the existence of a suitable state estimation scheme that estimates the position (p_n, p_e, h), the heading ψ, the airspeed V, the flight path angle γ, and the wind vector (w_n, w_e, w_h) [7].

If we assume coordinated turn conditions, then the kinematic equation of motion for the heading angle is given by

$$\dot{\psi} = \frac{g}{V}\tan\phi \tag{4}$$

where g is the magnitude of gravity at sea level. We assume in this paper that the roll and pitch dynamics are much faster than the heading and altitude dynamics, respectively, which implies that the roll and flight path angles can be considered as the control variables. Therefore, (3) and (4) become

$$\dot{h} = V\sin\gamma^c + w_h \tag{5}$$

$$\dot{\psi} = \frac{g}{V}\tan\phi^c \tag{6}$$

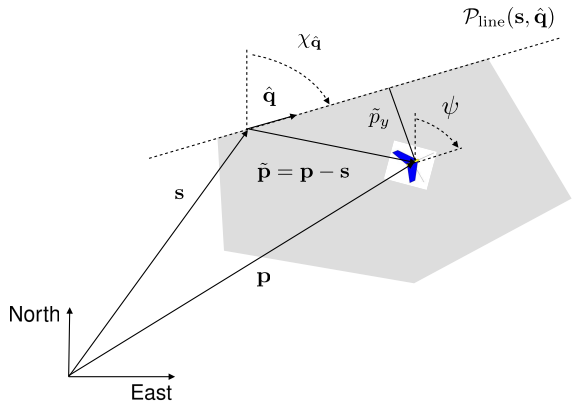

Fig. 1. This figure shows the configuration of the UAV indicated by $(\mathbf{p}, \psi)$, and the configuration of the UAV relative to $\mathcal{P}_{\text{line}}$ indicated by $(\tilde{\mathbf{p}}, \tilde{\psi})$.

where we will assume that the commanded roll angle is limited by $|\phi^c| \leq \phi_{\max} < \pi/2$ and that the commanded flight path angle is limited by $|\gamma^c| \leq \gamma_{\max} < \pi/2$.

III. Straight-Line Path Following

For a straight-line path, we will assume that the path is described by two vectors in $\mathbb{R}^3$, namely

$$\mathcal{P}_{\text{line}}(\mathbf{s},\hat{\mathbf{q}}) = \left\{\mathbf{r} \in \mathbb{R}^3 : \mathbf{r} = \mathbf{s} + \alpha\hat{\mathbf{q}}, \quad \alpha \in \mathbb{R}\right\}$$

where $\mathbf{s} = (s_n, s_e, s_d)^T$ is the inertially referenced origin of the path, and $\hat{\mathbf{q}} = (q_n, q_e, q_d)^T$ is a unit vector whose direction indicates the desired direction of travel referenced to the inertial frame. The desired course angle of the path is defined by

$$\chi_{\hat{\mathbf{q}}} \triangleq \text{atan2}(q_e, q_n)$$

where atan2 is the four quadrant inverse tangent function, and the desired flight path angle of the path is defined by

$$\gamma_{\hat{\mathbf{q}}} \triangleq \tan^{-1}\left(\frac{-q_d}{\sqrt{q_n^2 + q_e^2}}\right).$$

Fig. 1 shows the straight-line path $\mathcal{P}_{\text{line}}(\mathbf{s},\hat{\mathbf{q}})$, and the position of the UAV $\mathbf{p}$. The position of the UAV relative to $\mathcal{P}_{\text{line}}$ is given by $\tilde{\mathbf{p}} \triangleq \mathbf{p} - \mathbf{s}$. The heading of the UAV relative to $\mathcal{P}_{\text{line}}$ is given by $\tilde{\psi} = \psi - \chi_{\hat{\mathbf{q}}}$, where $\chi_{\hat{\mathbf{q}}}$ is the inertial heading of $\hat{\mathbf{q}}$ relative to north. To simplify the notation, we express the lateral dynamics in the path frame, by defining

$$\begin{pmatrix}\tilde{p}_x \\ \tilde{p}_y\end{pmatrix} = \begin{pmatrix}\cos\chi_{\hat{\mathbf{q}}} & \sin\chi_{\hat{\mathbf{q}}} \\ -\sin\chi_{\hat{\mathbf{q}}} & \cos\chi_{\hat{\mathbf{q}}}\end{pmatrix}\begin{pmatrix}p_n - s_n \\ p_e - s_e\end{pmatrix}.$$

Differentiating, we obtain

$$\dot{\tilde{p}}_x = V\cos\tilde{\psi}\cos\gamma + w_x \tag{7}$$
$$\dot{\tilde{p}}_y = V\sin\tilde{\psi}\cos\gamma + w_y \tag{8}$$

where $\tilde{p}_x$ is the projected distance along the path, $\tilde{p}_y$ is the cross-track error, w_x is the wind along the path, and w_y is the wind in the cross-track direction. We assume throughout this paper that the wind vector is known.

A. Lateral Guidance Law for Path Following

We will derive the guidance law for following a straight path by decoupling the lateral and longitudinal motion. For the lateral motion, we assume that γ is a constant. The lateral error dynamics are given by (8) and (6).

Our approach is derived using the theory of nested saturations [15], [16]. The objective is to drive $\tilde{p}_y$ and $\dot{\tilde{p}}_y$ to zero while simultaneously satisfying the constraint that $|\phi^c| \leq \phi_{\max}$. The first step in deriving the control strategy is to differentiate (8) to obtain

$$\ddot{\tilde{p}}_y = g\cos\tilde{\psi}\cos\gamma\tan\phi^c.$$

Define $W_1 = 1/2\dot{\tilde{p}}_y^2$ and differentiate to obtain

$$\dot{W}_1 = \dot{\tilde{p}}_y g\cos\tilde{\psi}\cos\gamma\tan\phi^c \tag{9}$$

and choose

$$\tan\phi^c = -\sigma_{M_1}\left(\frac{k_1\dot{\tilde{p}}_y + \sigma_{M_2}(\zeta)}{g\cos\tilde{\psi}\cos\gamma}\right) \tag{10}$$

where σ_{M_i} is the saturation function

$$\sigma_{M_i}(u) \triangleq \begin{cases} M_i, & \text{if } u > M_i \\ -M_i, & \text{if } u < -M_i \\ u, & \text{otherwise}\end{cases}$$

$k_1 > 0$, and M_1, M_2, and ζ will be selected in the discussion that follows. Substituting (10) into (9), gives

$$\dot{W}_1 = -\dot{\tilde{p}}_y g\cos\tilde{\psi}\cos\gamma\,\sigma_{M_1}\left(\frac{k_1\dot{\tilde{p}}_y + \sigma_{M_2}(\zeta)}{g\cos\tilde{\psi}\cos\gamma}\right)$$

which is negative when $|\tilde{\psi}| \leq \tilde{\psi}_{\max} < \pi/2$, $|\gamma| \leq \gamma_{\max} < \pi/2$, and $|\dot{\tilde{p}}_y| > M_2/k_1$. Therefore, if we guarantee that $|\tilde{\psi}| \leq \tilde{\psi}_{\max}$ and $|\gamma| \leq \gamma_{\max}$, then by the ultimate boundedness theorem [20], there exists a time T_1 such that for all $t \geq T_1$ we have that $|\dot{\tilde{p}}_y| \leq M_2/k_1$. If we also select M_1 and M_2 to satisfy

$$M_1 \geq \frac{2M_2}{g\cos\tilde{\psi}\cos\gamma} \tag{11}$$

then for all $t \geq T_1$, the signal in $\sigma_{M_1}(\cdot)$ is not in saturation and

$$\dot{W}_1 = -k_1\dot{\tilde{p}}_y^2 - \dot{\tilde{p}}_y\sigma_{M_2}(\zeta). \tag{12}$$

Define $z \triangleq k_1\tilde{p}_y + \dot{\tilde{p}}_y$, and $W_2 = 1/2z^2$, and differentiate W_2 to obtain

$$\dot{W}_2 = k_1 z\dot{\tilde{p}}_y - zg\cos\tilde{\psi}\cos\gamma\,\sigma_{M_1}\left(\frac{k_1\dot{\tilde{p}}_y + \sigma_{M_2}(\zeta)}{g\cos\tilde{\psi}\cos\gamma}\right).$$

If we let $\zeta = k_2 z$ where $k_2 > 0$, then for all $t \geq T_1$, we have

$$\dot{W}_2 = k_1 z\dot{\tilde{p}}_y - k_1 z\dot{\tilde{p}}_y - z\sigma_{M_2}(k_2 z) = -z\sigma_{M_2}(k_2 z)$$

which is negative definite. Therefore, we are guaranteed that $z = k_1\tilde{p}_y + \dot{\tilde{p}}_y \to 0$. Using the standard result on input-to-state stability [20], (12) guarantees that $\dot{\tilde{p}}_y \to 0$. Since both $z = k_1\tilde{p}_y + \dot{\tilde{p}}_y$ and $\dot{\tilde{p}}_y$ converge to zero, we can conclude that $\tilde{p}_y \to 0$.

To ensure that $|\phi|^c \leq \phi_{\max}$, set $M_1 = \tan\phi_{\max}$. To satisfy (11), we also need to constrain $\tilde{\psi}$ and γ. The constraint on γ will be discussed in Section III-B. For $\tilde{\psi}$, note that if $\phi^c = \phi_{\max}$, then $\dot{\tilde{\psi}} = g/V\tan\phi_{\max}$ and $\tilde{\psi}$ increases monotonically. Similarly, if $\phi^c = -\phi_{\max}$, then $\tilde{\psi}$ decreases monotonically. Therefore, if we can find $\tilde{\psi}_{\max} < \pi/2$ such that the set $B_{\tilde{\psi}_{\max}} \triangleq \left\{|\tilde{\psi}| \leq \tilde{\psi}_{\max}\right\}$ is positively invariant, then we could use the strategy given in (13), shown at the bottom of the page, for straight line tracking.

To find $\tilde{\psi}_{\max}$, let $W_3 = 1/2\tilde{\psi}^2$ and differentiate to obtain

$$\dot{W}_3 = \frac{g}{V}\tilde{\psi}\tan\phi^c = -\frac{g}{V}\tilde{\psi}\tan\left(\sigma_{M_1}\left(\frac{k_1(V\sin\tilde{\psi}\cos\gamma + w_y) + \sigma_{M_2}(k_2 z)}{g\cos\tilde{\psi}\cos\gamma}\right)\right). \quad (14)$$

Equation (14) is negative if $\left|k_1 V\sin\tilde{\psi}\cos\gamma\right| > k_1 w_{y,\max} + M_2$, where $w_{y,\max}$ is the maximum expected cross-track wind speed. Assuming that $\cos\gamma > 0$, this expression is true if

$$\sin\tilde{\psi}_{\max} = \frac{w_{y,\max} + \frac{M_2}{k1}}{V\cos\gamma_{\max}} \quad (15)$$

where $\gamma_{\max}$ is a parameter that will be specified in the following section.

Since $M_1 = \tan\phi_{\max}$, (11) implies that M_2 must be selected so that

$$M_2 \leq \frac{g}{2}\tan\phi_{\max}\cos\tilde{\psi}\cos\gamma.$$

Therefore, we select M_2 as

$$M_2 = \frac{g}{2}\tan\phi_{\max}\cos\tilde{\psi}_{\max}\cos\gamma_{\max}.$$

Substituting into (15) and rearranging gives

$$-\left(\frac{g}{2k_1}\tan\phi_{\max}\cos\gamma_{\max}\right)\cos\tilde{\psi}_{\max} + (V\cos\gamma_{\max})\sin\tilde{\psi}_{\max} = w_{y,\max}. \quad (16)$$

Using the trigonometric identity

$$A\cos\lambda + B\sin\lambda = C \Rightarrow \lambda = -\tan^{-1}\frac{A}{B} + \sin^{-1}\frac{C}{\sqrt{A^2+B^2}}$$

we obtain

$$\tilde{\psi}_{\max} = \tan^{-1}\left(\frac{g}{2k_1 V}\tan\phi_{\max}\right) + \sin^{-1}\left(\frac{w_{y,\max}}{\cos\gamma_{\max}\sqrt{\left(\frac{g}{2k_1}\tan\phi_{\max}\right)^2 + V^2}}\right). \quad (17)$$

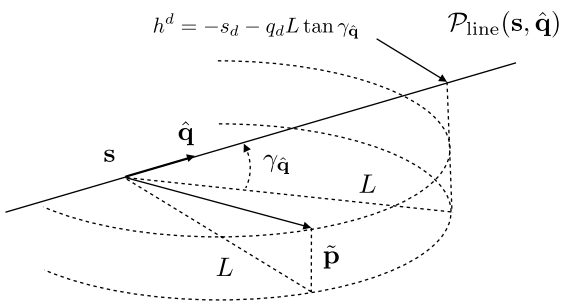

Fig. 2. Desired altitude along the waypoint path is found by projecting the position error of the UAV onto the north–east plane. The length of the projection L is used to find the point on the waypoint path that also projects onto the north–east plane a distance L from $\mathbf{s}$ and using the altitude at that point.

Therefore, we have the following theorem.

Theorem 3.1: Suppose that $k_1 > 0$, V, $\phi_{\max}$, $\gamma_{\max}$, and $w_{y,\max}$ are such that $\tilde{\psi}_{\max}$ in (17) is strictly less than $\pi/2$, and suppose that k_2, M_1 and M_2 are selected as:

1) $k_2 > 0$;
2) $M_1 = \tan\phi_{\max}$;
3) $M_2 = \frac{g}{2}\tan\phi_{\max}\cos\tilde{\psi}_{\max}\cos\gamma_{\max}$

then the commanded roll angle given by (13), results in system trajectories such that $\left|\tilde{p}_y(t)\right| + \left|\dot{\tilde{p}}(t)\right| \to 0$, and $|\phi^c(t)| \leq \phi_{\max}$. Note that the constraint that $\tilde{\psi}_{\max} < \pi/2$ essentially limits the maximum size of the wind that can be asymptotically rejected using (13). From (16), we observe that the upper bound on the wind is given by

$$\bar{w}_{y,\max} = V\cos\gamma_{\max}$$

which represents the projection of the velocity vector onto the horizontal plane, and therefore makes complete intuitive sense.

B. Longitudinal Guidance Law for Path Following

In this section, we develop a longitudinal guidance law for tracking the altitude portion of the waypoint path, where the longitudinal kinematics are given by (5).

The desired altitude for the UAV is found by projecting its current position relative to the waypoint path onto the north–east plane, as shown in Fig. 2 and finding the distance to this point, which is given by

$$L = \sqrt{\tilde{p}_x^2 + \tilde{p}_y^2}.$$

The position on the waypoint path that, when projected onto the north–east plane, also results in a distance L is given by

$$\mathbf{z} = \mathbf{s} + \hat{\mathbf{q}}L\tan\gamma_{\hat{\mathbf{q}}}.$$

$$\phi^c = \begin{cases} \phi_{\max}, & \text{if } \tilde{\psi} < -\tilde{\psi}_{\max} \\ -\phi_{\max}, & \text{if } \tilde{\psi} > \tilde{\psi}_{\max} \\ -\tan^{-1}\left[\sigma_{M_1}\left(\dfrac{k_1\dot{\tilde{p}}_y + \sigma_{M_2}\left(k_2\left(k_1\tilde{p}_y + \dot{\tilde{p}}_y\right)\right)}{g\cos\tilde{\psi}\cos\gamma}\right)\right], & \text{otherwise} \end{cases} \quad (13)$$

The down component of this vector is used to obtain the desired altitude as

$$h^d = -s_d - q_d L \tan\gamma_{\hat{\mathbf{q}}}. \tag{18}$$

The time derivative of h^d is given by

$$\begin{aligned}\dot{h}^d = &-q_d \tan\gamma_{\hat{\mathbf{q}}} V \frac{\tilde{p}_x \cos\tilde{\psi}\cos\gamma + \tilde{p}_y \sin\tilde{\psi}\cos\gamma}{\sqrt{\tilde{p}_x^2+\tilde{p}_y^2}} \\ &-q_d \tan\gamma_{\hat{\mathbf{q}}} \frac{\tilde{p}_x w_x + \tilde{p}_y w_y}{\sqrt{\tilde{p}_x^2+\tilde{p}_y^2}}.\end{aligned} \tag{19}$$

Define $W_4 = 1/2(h-h^d)^2$ and differentiate to obtain

$$\begin{aligned}\dot{W}_4 &= (h-h^d)(\dot{h}-\dot{h}^d) \\ &= (h-h^d)(V\sin\gamma^c + w_h - \dot{h}^d).\end{aligned}$$

If we select γ^c so that

$$V\sin\gamma^c + w_h - \dot{h}^d = -\sigma_{M_3}(k_3(h-h^d))$$

or in other words

$$\gamma^c = \sin^{-1}\left(\frac{\dot{h}^d - w_h - \sigma_{M_3}(k_3(h-h^d))}{V}\right) \tag{20}$$

then $\dot{W}_4 = -(h-h^d)\sigma_{M_3}(k_3(h-h^d))$ is negative definite.

To ensure that $|\gamma^c| \le \gamma_{\max}$, note that

$$\begin{aligned}\left|\dot{h}^d\right| \le &\left|-q_d\tan\gamma_{\hat{\mathbf{q}}} V \frac{\tilde{p}_x\cos\tilde{\psi}\cos\gamma + \tilde{p}_y\sin\tilde{\psi}\cos\gamma}{\sqrt{\tilde{p}_x^2+\tilde{p}_y^2}}\right| \\ &+\left|-q_d\tan\gamma_{\hat{\mathbf{q}}}\frac{\tilde{p}_x w_x+\tilde{p}_y w_y}{\sqrt{\tilde{p}_x^2+\tilde{p}_y^2}}\right| \\ \le\ & V\left|q_d\tan\gamma_{\hat{\mathbf{q}}}\right|\frac{|\tilde{p}_x|+|\tilde{p}_y|}{\sqrt{\tilde{p}_x^2+\tilde{p}_y^2}} \\ &+\left|q_d\tan\gamma_{\hat{\mathbf{q}}}\right|\frac{\sqrt{\tilde{p}_x^2+\tilde{p}_y^2}\sqrt{w_x^2+w_y^2}}{\sqrt{\tilde{p}_x^2+\tilde{p}_y^2}} \\ =\ & \sqrt{2}V\left|q_d\tan\gamma_{\hat{\mathbf{q}}}\right| + \left|q_d\tan\gamma_{\hat{\mathbf{q}}}\right|\sqrt{w_x^2+w_y^2}\end{aligned}$$

where we have used the fact that $\|\cdot\|_1 \le \sqrt{2}\,\|\cdot\|_2$. Therefore

$$\begin{aligned}\left|\frac{\dot{h}^d - w_h - \sigma_{M_3}\left(k_3(h-h^d)\right)}{V}\right| &\le \frac{|\dot{h}^d|}{V} + \frac{|w_h|}{V} + \frac{M_3}{V} \\ \le \sqrt{2}\left|q_d\tan\gamma_{\hat{\mathbf{q}}}\right| &+ \frac{\left|q_d\tan\gamma_{\hat{\mathbf{q}}}\right|\sqrt{w_x^2+w_y^2}+|w_h|}{V} + \frac{M_3}{V}.\end{aligned}$$

If M_3 is selected as

$$\begin{aligned}M_3 = &\ V\sin\gamma_{\max} - \sqrt{2}V\left|q_d\tan\gamma_{\hat{\mathbf{q}}}\right| \\ &-\left(\left|q_d\tan\gamma_{\hat{\mathbf{q}}}\right|\sqrt{w_x^2+w_y^2}+|w_h|\right)\end{aligned} \tag{21}$$

then from (20), we have that $|\gamma^c| \le \gamma_{\max}$. To ensure that $M_3 > 0$ we require that $\gamma_{\max}$ and $\gamma_{\hat{\mathbf{q}}}$ satisfy

$$\sin\gamma_{\max} > \sqrt{2}\left|q_d\tan\gamma_{\hat{\mathbf{q}}}\right| + \frac{\left|q_d\tan\gamma_{\hat{\mathbf{q}}}\right|\sqrt{w_x^2+w_y^2}+|w_h|}{V}. \tag{22}$$

Theorem 3.2 summarizes the results.

TABLE I
SIMULATION PARAMETERS USED FOR LATERAL PATH FOLLOWING

Parameter	Value	Range
Path origin $\mathbf{r}$	$(0,0,100)^T\ m$	-
Path direction $\hat{\mathbf{q}}$	$(1.00,1.00,-0.06)^T\ m$	-
Path velocity	$13\ m/s$	-
UAV initial position	$(50,0,0)^T\ m$	-
Simulation time	$30\ s$	-
k_1	0.30	0.10 - 0.55
k_2	0.30	0.10 - 1.45
$\phi_{\max}$	45°	25° - 70°
$\gamma_{\max}$	35°	15° - 60°
k_3	1.00	0.20 - 2.00
$w_{y,\max}$	$3\ m/s$	Constant

Theorem 3.2: Suppose that $\gamma_{\hat{\mathbf{q}}}$, V, and the wind vector are such that $\gamma_{\max}$ can be selected to satisfy both (22) and $\gamma_{\max} < \pi/2$, then if the commanded flight path angle is given by (20), where $k_3 > 0$, $\dot{h}^d$ is given by (19), and M_3 is given by (21), then $h \to h^d$ and $|\gamma^c(t)| \le \gamma_{\max}$, for all $t \ge 0$.

C. Simulation Results for Path Following

The simulation results are obtained using six 6 DOF nonlinear dynamic simulation, as explained in [7]. The effects of the different control parameters on the system response were tested by systematically increasing one parameter through 10 equally spaced values between the minimum and the maximum value while holding the other parameters constant. A description of the behavior is then given for each parameter. The parameters of interest for the straight-line path following are k_1, k_2, $\phi_{\max}$, $\gamma_{\max}$, and k_3. The guidance law is tested using an inclined line starting at the origin. The parameters for the simulation are shown in Table I. The nominal values for each parameter when not being tested through the range are shown in the value column of the table. These nominal values are the same values that are used on the actual UAV flight experiments.

1) Effects of Changing k_1: The gain k_1 affects the commanded roll angle ϕ^c by multiplying the error terms $\tilde{p}_y$ and $\dot{\tilde{p}}_y$. The effect of k_1 is dependent on the function σ_{M_2}. When the σ_{M_2} function is not in saturation, the numerator in σ_{M_1} becomes $(k_1+k_2)(\dot{\tilde{p}}_y+\tilde{p}_y)$, which shows that the gain k_1 has equal weight on both the error and the error rate and will increase the command which will increase the oscillations of the response. When the function σ_{M_2} is in saturation then k_1 has a larger effect on the error rate which adds damping to the lateral response of the vehicle. The gain k_1 also affects $\tilde{\psi}_{\max}$ in (17) but the contributions are less than the aforementioned effects. The effect of k_1 on ϕ^c of the UAV is shown in Fig. 3. The response time is decreased as k_1 increases but this comes with oscillations in ϕ^c.

2) Effects of Changing k_2: The gain k_2 enters into the commanded roll equation through the term $k_2(k_1\tilde{p}_y + \dot{\tilde{p}}_y)$, which is inside the function σ_{M_2}. Thus, the overall effect of

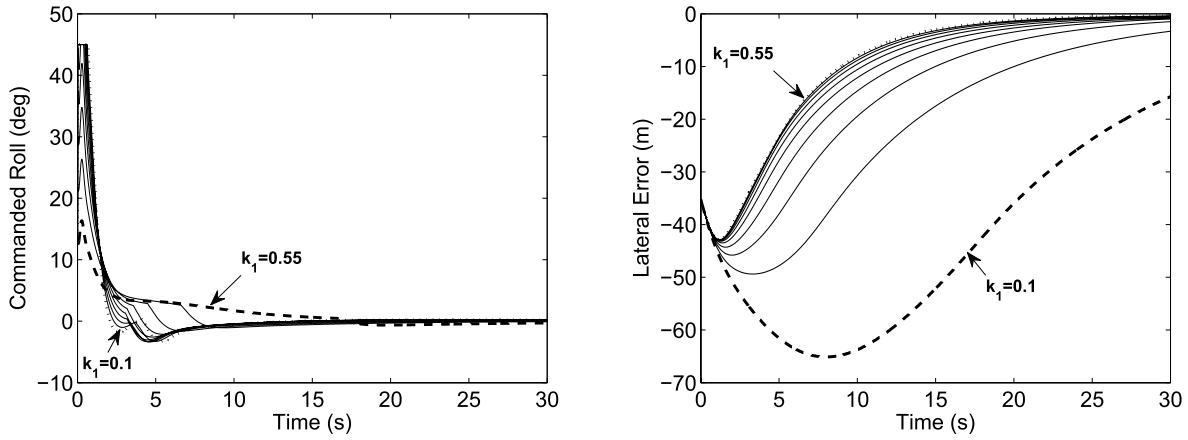

(a) (b)

Fig. 3. (a) Effect of changing the control gain k_1 on the commanded roll. (b) Effect of changing the control gain k_1 on the path error. For both subfigures, the dashed line corresponds to $k_1 = 0.10$ and the dotted line corresponds to $k_1 = 0.55$.

k_2 is limited in part to the saturation value of M_2. The effect of k_2 on the lateral response is also dependent on the value of k_1. If $k_1 < 1$ then k_2 has a larger effect on the error rate and will have an increased damping effect as k_2 is increased. If $k_1 > 1$ then k_2 has a larger effect on the lateral error but will have less effect on oscillations due to the saturation term M_2.

3) Effects of Changing $\phi_{\max}$: The parameter $\phi_{\max}$ affects the value of the saturation term M_1 through the term $\tan\phi_{\max}$. As $\phi_{\max}$ increases, M_1 also increases which allows the commanded roll to increase. This allows for more aggressive banking to return to the path.

4) Effects of Changing $\gamma_{\max}$: The term $\gamma_{\max}$ enters into the commanded roll equation in the saturation terms M_2 through the term $\cos\gamma_{\max}$. As $\gamma_{\max}$ increases, the saturation term M_2 also increases. This will add damping to the system if the gains $k_1 < 1$ and $k_2 < 1$ because the effect of $\tilde{p}_y$ will be decreased and the effect of $\dot{\tilde{p}}_y$ will be increased. $\gamma_{\max}$ also affects the longitudinal control. It affects the saturation term M_3 through the term $V\sin\gamma_{\max}$. As $\gamma_{\max}$ increases so does M_3. This causes γ^c to decrease. Therefore, increasing $\gamma_{\max}$ will decrease the response of the longitudinal control.

5) Effects of Changing k_3: The gain k_3 affects the commanded flight path angle by multiplying the term $h - h^d$, as observed in 20. As k_3 increases this will cause the commanded flight path angle to increase and error in height will decrease. The effect of changing k_3 on the longitudinal response is shown in Fig. 4.

If the wind vector is not known, or if we incorrectly estimate the wind, then the result will be a steady-state tracking error. The magnitude of the steady-state error is dependent on the magnitude of the wind, for example, a 2.2 m/s wind can cause a lateral off-path error of 6 m in simulation. An integrator could be added to the guidance law to remove the steady-state tracking error, when the wind vector is not known.

The simulation results show that the three parameters with the largest effect on the lateral response of the vehicle are k_1, k_2, and $\phi_{\max}$. The parameter $\phi_{\max}$ affects the response by saturating the command. If $\phi_{\max}$ is set properly, according to the airframe performance then the main parameters are k_1 and k_2. The longitudinal response is dominated by the effect of the gain k_3, as shown in Fig. 4.

D. Path Control Tuning for Straight-Line Path Following

There are five different parameters that are used in the lateral path control for straight-lines. For tuning purposes, the parameters $\tilde{\psi}_{\max}$, $\phi_{\max}$, and $\gamma_{\max}$ are chosen based on the capabilities of the airframe, leaving k_1 and k_2 that can be used to tune the response of the UAV. To start, the value of k_2 should be close to zero ($k_2 \approx 0.1$), then start with $k_1 = 1$ and if there is oscillation in the commanded roll, this should be made smaller. If there are no oscillations then the value of k_1 can be made larger. Once the value of k_1 has been chosen, the value of k_2 can be made larger until the desired response is achieved. The larger k_2 is, the faster the convergence to the path.

A similar approach is used for the longitudinal control. There are two parameters that can be changed to affect the response in height. These parameters are $\gamma_{\max}$ and k_3. The value for $\gamma_{\max}$ is chosen based on the capabilities of the airframe, and k_3 is tuned to achieve the desired response of the vehicle. The value of k_3 should start at 0.5 and be increased until the desired response is achieved.

IV. Orbit Following

A. Lateral Guidance Law for Orbit Following

In this section, we derive a guidance law to ensure asymptotic tracking of a circular orbit in wind. An orbital path is described by an inertially referenced center $\mathbf{c} = (c_n, c_e, c_d)^T$, a radius $\rho \in \mathbb{R}$, and a direction $\lambda \in \{-1, 1\}$, as

$$\mathcal{P}_{\text{orbit}}(\mathbf{c}, \rho, \lambda) = \{\mathbf{r} \in \mathbb{R}^3 : \mathbf{r} = \mathbf{c} + \lambda\rho \begin{pmatrix}\cos\varphi, & \sin\varphi & 0\end{pmatrix}^T, \varphi \in [0, 2\pi)\}$$

where $\lambda = 1$ signifies a clockwise orbit and $\lambda = -1$ signifies a counterclockwise orbit. We assume in this section that the longitudinal controller maintains a constant altitude. We also

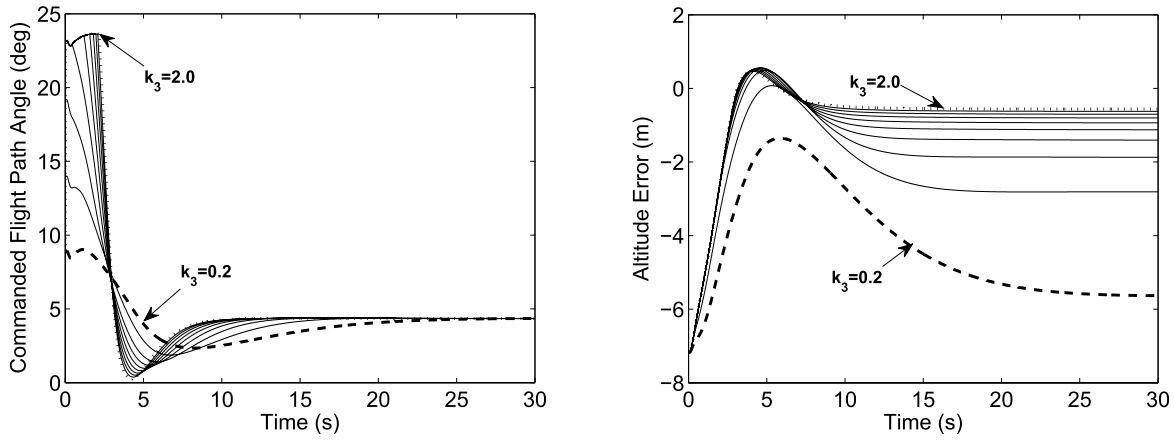

(a) (b)

Fig. 4. (a) Effect of changing k_3 on the commanded flight path angle. (b) Effect of changing k_3 on the altitude error. For both subfigures, the dashed line corresponds to $k_3 = 0.2$ and the dotted line corresponds to $k_3 = 2.0$.

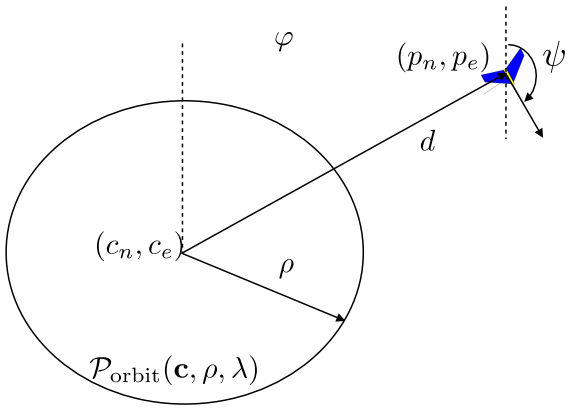

Fig. 5. Conversion from rectangular coordinates to polar coordinates for orbit following.

note that since the autopilot maintains a constant airspeed and since the wind is assumed to be constant, from (5) the air mass referenced flight path angle is constant and is given by $\gamma = -\sin^{-1}(w_h/V_a)$.

The guidance strategy for orbit following is best derived in polar coordinates. Let

$$d \triangleq \sqrt{(p_n - c_n)^2 + (p_e - c_e)^2}$$

be the lateral distance from the desired center of the orbit to the UAV, and let

$$\varphi \triangleq \text{atan2}\,(p_e - c_e, \quad p_n - c_n) \tag{23}$$

be the phase angle of the relative position, as shown in Fig. 5, where atan2 is the four quadrant inverse tangent function. Differentiating d and using (1) and (2) gives

$$\begin{aligned}\dot{d} &= \frac{(p_n - c_n)\dot{p}_n + (p_e - c_e)\dot{p}_e}{d} \\ &= \frac{(p_n - c_n)V\cos\psi\cos\gamma + (p_e - c_e)V\sin\psi\cos\gamma}{d} \\ &\quad + \frac{(p_n - c_n)w_n + (p_e - c_e)w_e}{d}.\end{aligned}$$

Defining the wind speed W and wind direction ψ_w so that

$$W\begin{pmatrix}\cos\psi_w \\ \sin\psi_w\end{pmatrix} \triangleq \begin{pmatrix}w_n \\ w_e\end{pmatrix}$$

and using (23) gives

$$\begin{aligned}\dot{d} &= V\cos\gamma\,\frac{(p_n - c_n)\cos\psi + (p_e - c_e)\sin\psi}{d} \\ &\quad + W\frac{(p_n - c_n)\cos\psi_w + (p_e - c_e)\sin\psi_w}{d} \\ &= V\cos\gamma\left(\frac{p_n - c_n}{d}\right)(\cos\psi + \sin\psi\tan\varphi) \\ &\quad + W\left(\frac{p_n - c_n}{d}\right)(\cos\psi_w + \sin\psi_w\tan\varphi) \\ &= V\cos\gamma\cos\varphi\,(\cos\psi + \sin\psi\tan\varphi) \\ &\quad + W\cos\varphi\,(\cos\psi_w + \sin\psi_w\tan\varphi) \\ &= V\cos\gamma\,(\cos\psi\cos\varphi + \sin\psi\sin\varphi) \\ &\quad + W\,(\cos\psi_w\cos\varphi + \sin\psi_w\sin\varphi) \\ &= V\cos\gamma\,\cos(\psi - \varphi) + W\cos(\psi_w - \varphi).\end{aligned}$$

Similarly, differentiating (23) and simplifying gives

$$\dot{\varphi} = \frac{V\cos\gamma}{d}\sin(\psi - \varphi) + \frac{W}{d}\sin(\psi_w - \varphi).$$

The orbital kinematics in polar coordinates are therefore given by

$$\begin{aligned}\dot{d} &= V\cos(\psi - \varphi)\cos\gamma + W\cos(\psi_w - \varphi) \\ \dot{\varphi} &= \frac{V}{d}\sin(\psi - \varphi)\cos\gamma + \frac{W}{d}\sin(\psi_w - \varphi) \\ \dot{\psi} &= \frac{g}{V}\tan\phi^c.\end{aligned}$$

As shown in Fig. 6, for a clockwise orbit, the desired course angle when the UAV is located on the orbit is given by $\psi^d = \varphi + \pi/2$.

Similarly, for a counterclockwise orbit, the desired angle is given by $\psi^d = \varphi - \pi/2$. Therefore, in general, we have

$$\psi^d = \varphi + \lambda\frac{\pi}{2}.$$

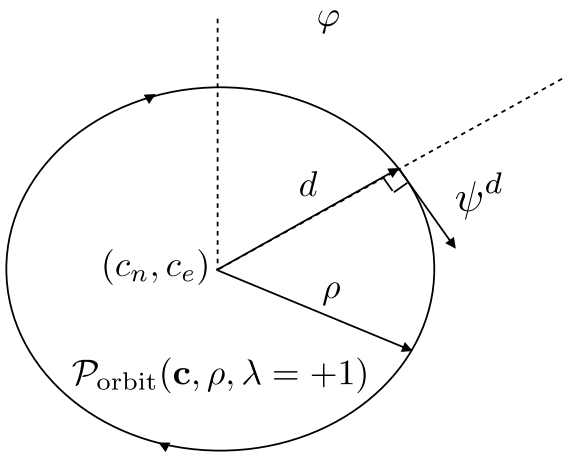

Fig. 6. Desired angle when the UAV is on the orbit is given by ψ^d.

Defining the error variables $\tilde{d} \triangleq d - \rho$ and $\tilde{\psi} \triangleq \psi - \psi^d$, the orbital kinematics can be restated as

$$\dot{\tilde{d}} = -\lambda V \sin\tilde{\psi}\cos\gamma + W\cos(\psi - \psi_w) \quad (24)$$

$$\dot{\tilde{\psi}} = \frac{g}{V}\tan\phi^c - \lambda\frac{V}{d}\cos\tilde{\psi}\cos\gamma - \frac{W}{d}\sin(\psi - \psi_w). \quad (25)$$

The control objective is to force $\tilde{d}(t) \to 0$ and $\dot{\tilde{d}}(t) \to 0$ while satisfying the input constraint $|\phi^c(t)| \le \phi_{\max}$.

Our approach to the orbit following guidance strategy is similar to the method followed in Section III-A with the added complication that we must deal with the inside of the orbit.

Following the exposition in Section III-A, differentiate (24) to obtain:

$$\begin{aligned}\ddot{\tilde{d}} &= -\lambda V\cos\tilde{\psi}\cos\gamma\,\dot{\tilde{\psi}} + W\sin(\psi - \psi_w)\dot{\psi}\\ &= -\lambda V\cos\gamma\cos\tilde{\psi}\\ &\quad\times\left(\frac{g}{V}\tan\phi^c - \lambda\frac{V}{d}\cos\gamma\cos\tilde{\psi} - \frac{W}{d}\sin(\psi - \psi_w)\right)\\ &\quad + W\sin(\psi - \psi_w)\left(\frac{g}{V}\tan\phi^c\right)\\ &= -\left(\lambda g\cos\tilde{\psi}\cos\gamma + g\frac{W}{V}\sin(\psi - \psi_w)\right)\\ &\quad\times\left(\tan\phi^c - \lambda\frac{V^2}{gd}\cos\tilde{\psi}\cos\gamma\right).\end{aligned}$$

Define $W_5 = 1/2\dot{\tilde{d}}^2$ and differentiate to obtain

$$\dot{W}_5 = -\dot{\tilde{d}}\left(\lambda g\cos\tilde{\psi}\cos\gamma + g\frac{W}{V}\sin(\psi - \psi_w)\right)\times\left(\tan\phi^c - \lambda\frac{V^2}{gd}\cos\tilde{\psi}\cos\gamma\right) \quad (26)$$

and choose ϕ^c as

$$\phi_c = \tan^{-1}\left[\lambda\frac{V^2}{gd}\cos\gamma\cos\tilde{\psi} + \sigma_{M_4}\left(\frac{k_4\dot{\tilde{d}} + \sigma_{M_5}(\zeta)}{\lambda g\cos\tilde{\psi}\cos\gamma + g\frac{W}{V}\sin(\psi - \psi_w)}\right)\right] \quad (27)$$

where $k_4 > 0$ is a control gain, and M_4, M_5, and ζ will be selected in the following discussion. Substituting (27) into (26) gives

$$\dot{W}_5 = -\dot{\tilde{d}}\left(\lambda g\cos\tilde{\psi}\cos\gamma + g\frac{W}{V}\sin(\psi - \psi_w)\right)\sigma_{M_4}\times\left(\frac{k_4\dot{\tilde{d}} + \sigma_{M_5}(\zeta)}{\lambda g\cos\tilde{\psi}\cos\gamma + g\frac{W}{V}\sin(\psi - \psi_w)}\right)$$

which is negative when $|\dot{\tilde{d}}| > M_5/k_4$. Therefore, by the ultimate boundedness theorem [20] there exists a time T_3 such that for all $t \ge T_3$, we have $|\dot{\tilde{d}}| \le M_5/k_4$. If we select M_4 and M_5 to satisfy

$$M_4 \ge \left|\frac{2M_5}{\lambda g\cos\tilde{\psi}\cos\gamma + g\frac{W}{V}\sin(\psi - \psi_w)}\right| \quad (28)$$

then for all $t \ge T_3$, the signal σ_{M_4} is not in saturation and

$$\dot{W}_5 = -k_4\dot{\tilde{d}}^2 - \dot{\tilde{d}}\sigma_{M_5}(\zeta). \quad (29)$$

Define $z_2 = k_4\tilde{d} + \dot{\tilde{d}}$ and $W_6 = 1/2z_2^2$, and differentiate W_6 to obtain

$$\dot{W}_6 = z_2k_4\dot{\tilde{d}} - z_2\left(\lambda g\cos\tilde{\psi}\cos\gamma + g\frac{W}{V}\sin(\psi - \psi_w)\right)\sigma_{M_4}\times\left(\frac{k_4\dot{\tilde{d}} + \sigma_{M_5}(\zeta)}{\lambda g\cos\tilde{\psi}\cos\gamma + g\frac{W}{V}\sin(\psi - \psi_w)}\right). \quad (30)$$

If we let $\zeta = k_5z_2$, where $k_5 > 0$ is a control gain, then for all $t \ge T_3$, we have

$$\dot{W}_6 = -z_2\sigma_{M_5}(k_5z_2) \quad (31)$$

which is negative definite. Therefore, we are guaranteed that $z_2 = k_4\tilde{d} + \dot{\tilde{d}} \to 0$. Using the standard result on input-to-state stability [20], (29) guarantees that $\dot{\tilde{d}} \to 0$. We can therefore conclude that $\tilde{d} \to 0$.

To satisfy the input saturation constraint, from (27), we require that

$$\tan\phi_{\max} \ge \frac{V^2}{dg}|\cos\gamma|\,|\cos\tilde{\psi}| + M_4.$$

If we ensure that when (27) holds, that $d \ge d_{\min}$ and that $|\tilde{\psi}| \le \tilde{\psi}_{\max}$, then a sufficient condition to avoid input saturation is that

$$\tan\phi_{\max} \ge \frac{V^2}{d_{\min}g}\cos\gamma_{\max}\cos\tilde{\psi}_{\max} + M_4.$$

Therefore, select

$$M_4 = \tan\phi_{\max} - \frac{V^2}{d_{\min}g}\cos\gamma_{\max}\cos\tilde{\psi}_{\max} \quad (32)$$

where to ensure that $M_4 > 0$ we require that $\phi_{\max}$, $d_{\min}$, $\tilde{\psi}_{\max}$ be selected so that

$$\tan\phi_{\max} > \frac{V^2}{d_{\min}g}\cos\gamma_{\max}\cos\tilde{\psi}_{\max}. \quad (33)$$

To satisfy constraint (28) select M_5 as

$$M_5 = \frac{1}{2}M_4g\left|\cos\tilde{\psi}_{\max}\cos\gamma_{\max} - \frac{W}{V}\right| \quad (34)$$

where the windspeed is required to satisfy

$$W < V \cos \tilde{\psi}_{\max} \cos \gamma_{\max}. \tag{35}$$

From (33), we observe that the roll command (27) can only be active when $|\tilde{\psi}| \leq \tilde{\psi}_{\max}$ and $d \geq d_{\min}$. The basic strategy will be to command a zero roll angle when $d < d_{\min}$ and to saturate the roll angle at $\pm\phi_{\max}$ when $|\tilde{\psi}| > \tilde{\psi}_{\max}$ in the direction that reduces $|\tilde{\psi}|$. Therefore, let

$$\phi^c = \begin{cases} 0, & \text{if } d < d_{\min} \\ -\lambda\phi_{\max}, & \text{if } (d \geq d_{\min}) \text{ and } (\lambda\tilde{\psi} \geq \tilde{\psi}_{\max}) \\ \lambda\phi_{\max}, & \text{if } (d \geq d_{\min}) \text{ and } (-\lambda\tilde{\psi} \geq \tilde{\psi}_{\max}) \\ \text{[Equation (27)]}, & \text{otherwise.} \end{cases} \tag{36}$$

The convergence result is summarized in the following theorem.

Theorem 4.1: If the commanded roll angle is given by (36), where:

1) $k_4 > 0$;
2) $\phi_{\max}$, $\gamma_{\max}$, and $\tilde{\psi}_{\max}$ are positive and strictly less than $\pi/2$;
3) $d_{\min}$ and ρ satisfy

$$\frac{V^2 + VW}{g \tan \phi_{\max}} < d_{\min} < \rho; \tag{37}$$

4) the magnitude of the wind satisfies (35);
5) M_4 is given by (32);
6) M_5 is given by (34);

then $|\phi^c(t)| \leq \phi_{\max}$, and $(d, \dot{d}) \to (\rho, 0)$.

Proof:

The orbital dynamics of the system can be written as

$$\dot{d} = -V \sin(\lambda\tilde{\psi}) \cos\gamma + W \cos(\psi - \psi_w) \tag{38}$$

$$\lambda\dot{\tilde{\psi}} = \frac{g}{V} \tan(\lambda\phi^c) - \frac{V}{d} \cos\tilde{\psi} \cos\gamma - \lambda\frac{W}{d} \sin(\psi - \psi_w) \tag{39}$$

where ϕ^c is given by (36). We will trace the trajectories of the system using the state variables $(d, \lambda\tilde{\psi})$ because the control action is explicitly defined with respect to these variables in (36). Note, however, that the equilibrium is at $(d, \dot{d})^\top = (\rho, 0)^\top$. Therefore, in the state variable $(d, \lambda\tilde{\psi})$ the equilibrium is actually time-varying. In particular, from (31) we note that the manifold define by $z_0 = 0$ is positively invariant, and that on the manifold $\dot{\tilde{d}} = -k_4\tilde{d}$, which implies that $\tilde{d} \to 0$, which implies that

$$-V \sin(\lambda\tilde{\psi}) \cos\gamma + W \cos(\psi - \psi_w) + k_4(d - \rho) = 0.$$

Solving for $\lambda\tilde{\psi}$ on the interval $\lambda\tilde{\psi} \in \left[-\tilde{\psi}_{\max}, \tilde{\psi}_{\max}\right]$ and noting that $\tilde{\psi}_{\max} < \pi/2$ gives

$$\lambda\tilde{\psi} = \sin^{-1}\left(\frac{k_4(d - \rho) + W \cos(\psi - \psi_w)}{V \cos\gamma}\right). \tag{40}$$

Therefore, in equilibrium, i.e., when $d = \rho$, we have

$$\lambda\tilde{\psi}^*(t) = \sin^{-1}\left(\frac{W \cos(\psi(t) - \psi_w)}{V \cos\gamma}\right). \tag{41}$$

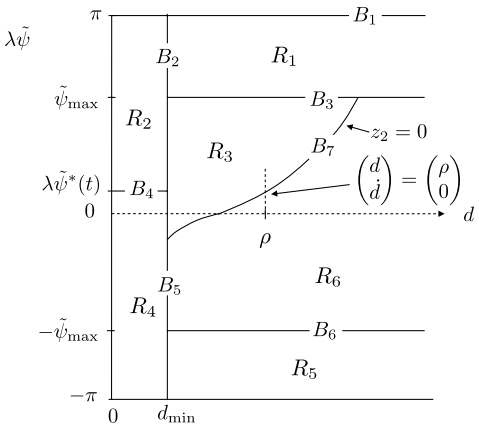

Fig. 7. State space for orbit following. Regions discussed in the proof are labeled R_i, and boundaries between regions are labeled B_i.

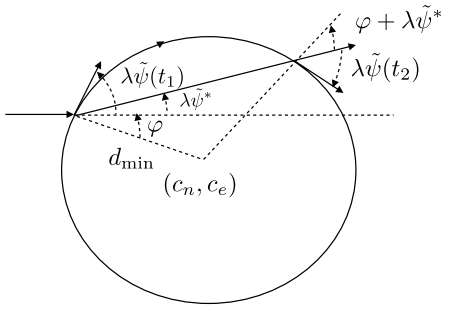

Fig. 8. In regions R_2 and R_4, the roll angle is zero and the vehicle drifts in the wind at a constant rate.

Of course this makes sense physically because the UAV must continuously change its crab angle as it transitions around the orbit to adjust for the wind.

Letting $d = d_{\min}$ in (40) gives

$$\lambda\tilde{\psi}^\dagger(t) \triangleq \sin^{-1}\left(\frac{k_4(d_{\min} - \rho) + W \cos(\psi - \psi_w)}{V \cos\gamma}\right). \tag{42}$$

Divide the state space into six regions, as shown in Fig. 7, where R_i denotes open regions of the state space, and B_i denote boundaries between the regions. We denote the closure of R_i as $\bar{R}_i$.

The proof amounts to a careful accounting of all possible trajectories of the system by showing the following statements.

Fact 1: All trajectories starting in $\bar{R}_1$, enter $R_2 \bigcup R_3 \bigcup R_6$ in finite time.

Fact 2: All trajectories starting in, or entering R_2 through boundary B_2, exit R_4 through B_5 in finite time, where B_2, B_4, and B_5 intersect at $(d_{\min}, \lambda\tilde{\psi}^*)$.

Fact 3: All trajectories starting in, or entering R_3, either converge to $(\rho, 0)$, or enter R_2 in finite time.

Fact 4: All trajectories starting in, or entering R_5, enter R_6 in finite time.

Fact 5: All trajectories starting in, or entering R_6, converge to $(\rho, 0)$.

Therefore, all trajectories in the system, converge to the equilibrium $(d, \dot{d})^\top = (\rho, 0)^\top$.

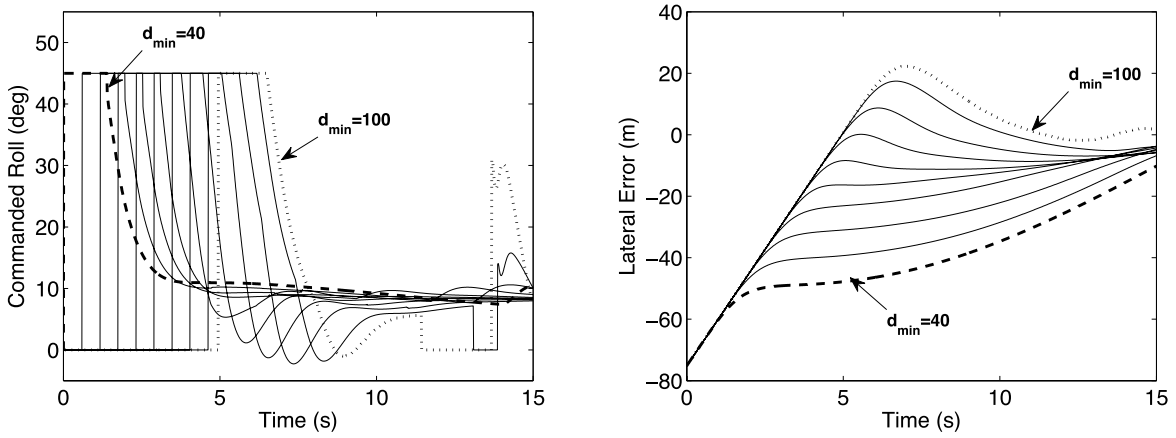

(a) (b)

Fig. 9. (a) Effect of changing $d_{\min}$ on the commanded roll. (b) Effect of changing $d_{\min}$ on the path error. For both subfigures, the dashed line corresponds to $d_{\min} = 40$ and the dotted line corresponds to $d_{\min} = 100$.

TABLE II
SIMULATION PARAMETERS USED FOR LATERAL PATH FOLLOWING

Parameter	Value	Range
Orbit origin $\mathbf{c}$	$(0,0,100)^T\ m$	-
Orbit direction λ	1	-
Orbit radius	$125\ m$	-
Orbit velocity	$15\ m/s$	-
UAV initial position	$(50,0,0)^T\ m$	-
Simulation time	$15\ s$	-
k_4	0.5	0.1 - 1.0
k_5	0.4	0.1 - 1.0
$\phi_{\max}$	45°	25° - 70°
$\gamma_{\max}$	35°	10° - 35°
$\tilde{\psi}_{\max}$	45°	25° - 70°
$d_{\min}$	70%	40% - 85%

TABLE III
PROPERTIES OF THE STRAIGHT-LINE PATH AND CONTROL PARAMETERS USED FOR EXPERIMENTAL TESTS

Parameter	Value
Line origin $\mathbf{r}$	$(-100,-200,100)^T\ m$
Line direction $\hat{\mathbf{q}}$	$(1,1,0)^T\ m$
Line velocity	$15\ m/s$
k_1	0.3
k_2	0.3
k_3	1.0
$\phi_{\max}$	45°
$\gamma_{\max}$	35°

Proof of Fact 1: In $\bar{R}_1$, we have

$$\lambda\dot{\tilde{\psi}} = -\frac{g}{V}\tan\phi_{\max} - \frac{V}{d}\cos(\lambda\tilde{\psi})\cos\gamma - \lambda\frac{W}{d}\sin(\psi - \psi_w).$$

Maximizing $\lambda\dot{\tilde{\psi}}$ on $\bar{R}_1$ over all possible values for $\gamma \in (-\pi/2, \pi/2)$ and $\psi - \psi_w \in (-\pi, \pi]$ gives

$$\max_{\bar{R}_1} \lambda\dot{\tilde{\psi}} = -\frac{g}{V}\tan\phi_{\max} + \frac{V}{d_{\min}} + \frac{W}{d_{\min}}.$$

Condition 37 ensures that $\max_{\bar{R}_1} \lambda\dot{\tilde{\psi}}$ is bounded above by a negative constant. Therefore, all trajectories starting in $\bar{R}_1$ leave $\bar{R}_1$ in finite time.

Proof of Fact 2: In R_2 and R_4, the roll command is $\phi^c = 0$, which implies that the heading rate is zero. The drift angle due to wind is given by (41). The geometry is shown in Fig. 8, where it can be observed that when the vehicle enters $d_{\min}$, we have $\varphi + \tilde{\psi}(t_1) = \pi/2$, and when it exits $d_{\min}$, we have $\varphi + \lambda\tilde{\psi}^* - \lambda\tilde{\psi}(t_2) = \pi/2$, therefore

$$\lambda\tilde{\psi}(t_2) = -\lambda\tilde{\psi}(t_1) + \lambda\tilde{\psi}^*.$$

This implies that trajectories in R_2 and R_4 are symmetric about boundary B_4, and therefore all trajectories entering or starting in R_3 enter R_4 and then leave R_4 through B_5 in finite time.

Proof of Fact 3. In R_3, the trajectories of the system are given by (38) and (30). Using the argument immediately following (30), we know that trajectories that stay in R_3 will eventually converge to $(d, \dot{d})^\top = (\rho, 0)^\top$. Therefore, trajectories either converge to $(\rho, 0)^\top$ or leave R_3 in finite time. Since by the proof of Fact 1 trajectories that leave R_3 cannot enter R_1, and by the proof of Fact 2 they cannot enter R_4, and since the invariance of B_7 prevents trajectories entering into R_6, all trajectories that do not converge to $(\rho, 0)^\top$ must enter R_2 in finite time.

Proof of Fact 4: Similar to the proof of Fact 1.

Proof of Fact 5: The argument is similar to the proof of Fact 2 with the exception that trajectories cannot leave R_6 through B_3 (proof of Fact 1), B_5 (proof of Fact 2), or B_6 (proof of Fact 4). Therefore, all trajectories in R_6 converge to $(\rho, 0)$. ■

(a) (b)

Fig. 10. (a) Small UAV used for testing. (b) Autopilot used for control.

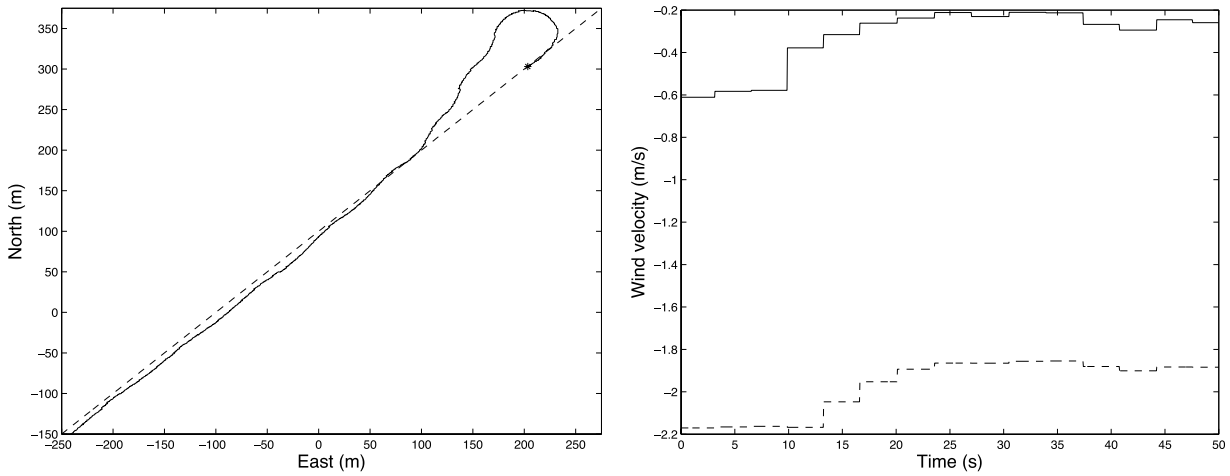

(a) (b)

Fig. 11. (a) Desired versus actual path of the UAV. The desired path is dashed. (b) Estimated wind during flight. Dashed line shows the north wind, and solid line shows the east wind.

B. Simulation Results for Orbit Following

The effects of different control parameters for orbit following are tested similar to straight-line following discussed in Section III. The plots are not shown here because of the similarity of effects with the parameters used in the line following. A short discussion follows for clarity. The parameters of interest are k_4, k_5, $\tilde{\psi}_{\max}$, $\phi_{\max}$, and $d_{\min}$. If we choose $\phi_{\max}$ and $\tilde{\psi}_{\max}$ as parameters then $d_{\min}$ must be chosen such that (33) is satisfied. The value of $d_{\min}$ is chosen as a percentage of the orbit radius while still satisfying the inequality. Table II shows the orbit parameters and the nominal control parameters used in the simulation. The nominal values are the same values that are used on the actual UAV flight experiments. The orbit is a flat orbit with constant desired velocity.

1) Effects of Changing Parameters: The effects of changing the parameters for the orbit control have similar effects on the UAV response as those of the parameters for the line control as explained above in Section III-C. The effects of changing gain k_4 for the orbit control is similar to the effect of k_1 for line control, k_5 is similar to k_2 and the angles also have similar effects ($\phi_{\max}$ and $\gamma_{\max}$). The parameter $\tilde{\psi}_{\max}$ has the same effect on the response as the parameter $\gamma_{\max}$. However, the parameter $d_{\min}$ is not used in the straight-line path control so this parameter will be discussed in more detail here.

2) Effects of Changing $d_{\min}$: The parameter $d_{\min}$ affects the commanded roll in two ways. First, the commanded roll is zero if the UAV is inside $d_{\min}$. Therefore, if $d_{\min}$ is increased closer to the actual orbit radius ρ the UAV will not start to turn until it is closer to the orbit and will therefore overshoot the orbit. The second way that $d_{\min}$ enters into the commanded roll equation is through the saturation term M_4 in (32). As $d_{\min}$ is increased it will also increase the saturation term M_4 and will increase the overall commanded roll. This increase in commanded roll will increase the rate of convergence to the path. The effects of $d_{\min}$ on the response of the UAV are shown in Fig. 9. As shown in the plot, having a large $d_{\min}$ will increase the rate of convergence but simultaneously starts to increase the overshoot by delaying the point at which the UAV starts to turn. Therefore, as $d_{\min}$ continues to increase above 70% the rate of convergence increases but the overall quality of the response declines because of the increase in overshoot. As $d_{\min}$ approaches 100%, anytime the UAV is inside the orbit the commanded roll will be set to zero. This creates undesirable effects as the UAV will oscillate in and out of the orbit due

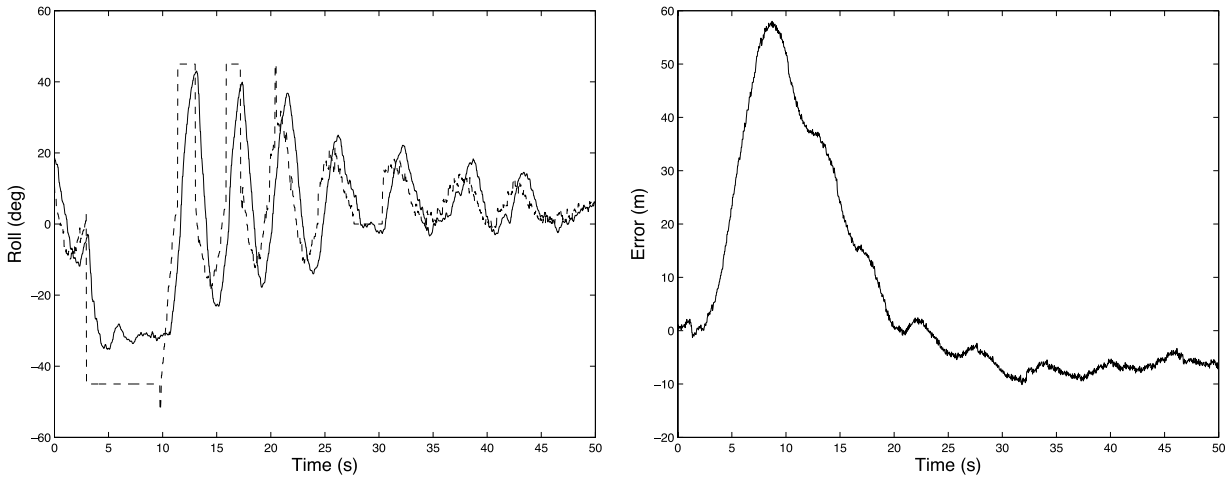

(a) (b)

Fig. 12. (a) Desired versus actual roll angles of the UAV. Dashed line shows the desired roll. (b) Path error of the UAV during flight.

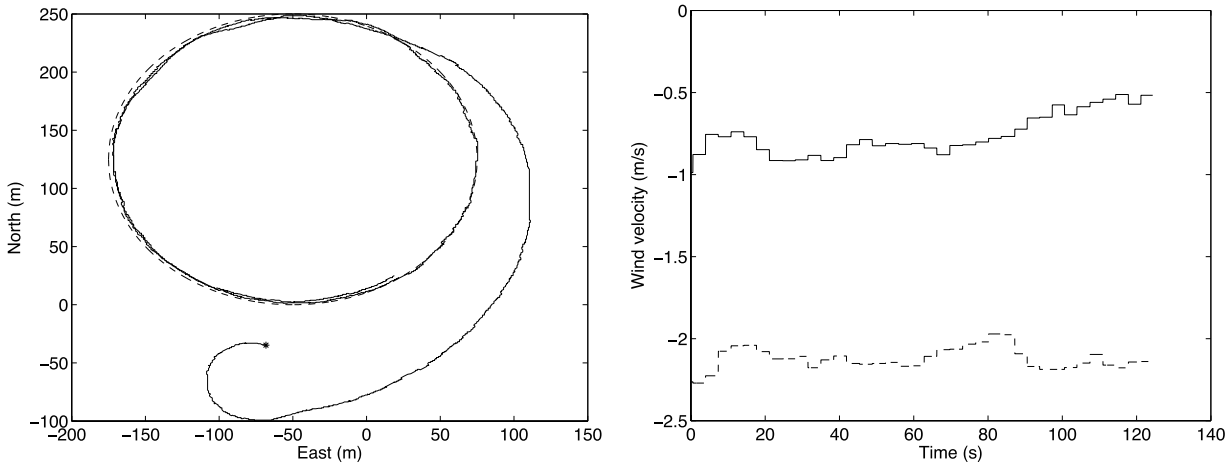

(a) (b)

Fig. 13. (a) Desired versus actual path of the UAV. Dashed line shows the desired path, and solid line shows the actual path. (b) Estimated wind during flight. North wind is dashed and east wind is solid.

to the value of $d_{\min}$ being close to the orbit radius ρ. This behavior is shown for the two larger values of $d_{\min}$ where the commanded roll is immediately set to zero in Fig. 9(a).

C. Path Control Tuning for Orbit Path Following

Similar methods are used to tune the orbit path controller, as were described in Section III-D, where the effects of k_4 on the orbit control are similar to the effects of k_1 and the effects of k_5 are similar to that of k_2 and the other parameters are chosen based on the vehicle airframe.

V. Experimental Result

The nested saturation control law was tested on the UAV shown in Fig. 10(a). The UAV is equipped with a Lockheed Martin Procerus Technologies Kestrel autopilot shown in Fig. 10(b), a uBlox GPS receiver, and another separate processor, which contains the control algorithm that communicates with the autopilot. The onboard autopilot communicates with a ground station computer using Virtual Cockpit 3-D. The communication between the UAV and the ground station is done using the Lockheed Martin Procerus Technologies Ground Control Station with Microhard Nano modems which use a frequency of 900 MHz. The desired velocity, altitude and other path information is controlled by the user at the ground station and is transmitted to the UAV during flight. The autopilot uses the GPS signal, the onboard inertial measurement unit, differential and absolute pressure sensors, and the onboard magnetometer to calculate the position, orientation, heading, and flight path angle of the vehicle, as well as the components of the wind. We note that to estimate the wind vector the vehicle must maneuver with respect to the air mass. If the mission scenario does not require such maneuvering, then the wind may need to be estimated prior to the start of the mission. The state information along with the desired

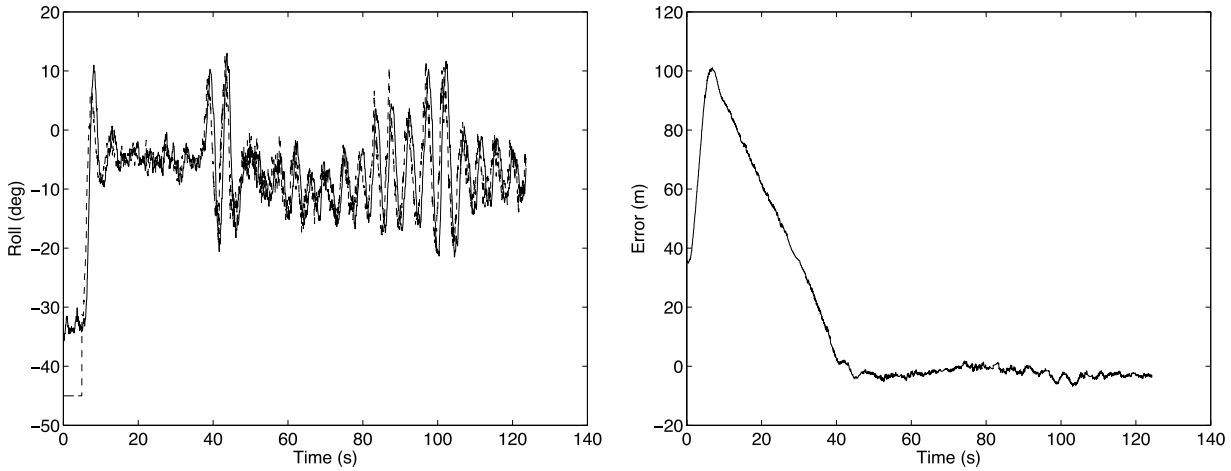

(a) (b)

Fig. 14. (a) Desired versus actual roll angles of the UAV. Dashed line shows the desired path, and solid line shows the actual path. (b) Path error of the UAV during flight.

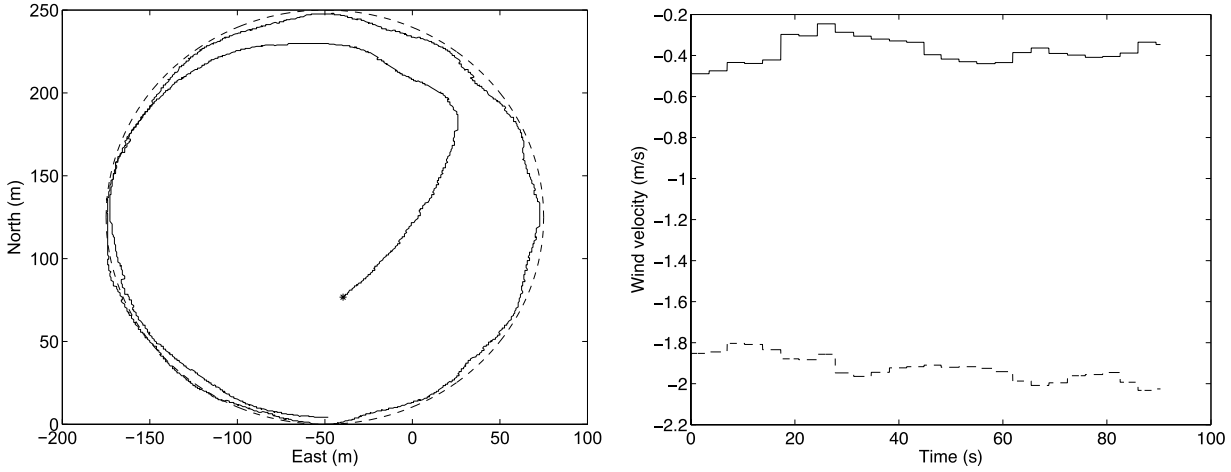

(a) (b)

Fig. 15. (a) Desired versus actual path of the UAV. Dashed line shows the desired path, and solid line shows the actual path. (b) Estimated wind during flight. Dashed line shows the north wind, and solid line shows the east wind.

path information is passed to the processor running the control algorithm. The nested saturation control law is then used to calculate the desired velocity, desired roll angle, and the desired flight-path angle. These commanded values are then sent to the autopilot, which performs the low-level control.

The controller was tested on the hardware for both straight-line paths and circular orbits. All of the paths tested were a constant altitude of 100 m above ground level while the desired velocity was a constant 15 m/s. A variety of initial conditions were tested to evaluate the response of the proposed control method.

A. Path Following Results

The properties of the straight-line path and the control parameters used for the flight are shown in Table III. For the experimental results, the wind speed was assumed to be zero, which will result in steady-state tracking errors.

Figs. 11 and 12 show the results from the UAV flying the along the straight-line. The vehicle was initially flying along the line in the positive north and east directions. The commanded direction along the same line was then reversed and the vehicle had to switch directions and return to the desired line. Fig. 12(a) shows the desired and actual roll angles.

B. Orbit Following Results

The orbit properties and corresponding control parameters used to fly the orbit are shown in Table IV.

Two different initial conditions were used in the experiments for orbit following. In the first case, the initial position is outside the desired orbit and the heading is opposite the desired heading. The results for this case are shown in Figs. 13 and 14. In the second case, the initial position is inside the desired orbit and is inside $d_{\min}$. The results for this case are shown in

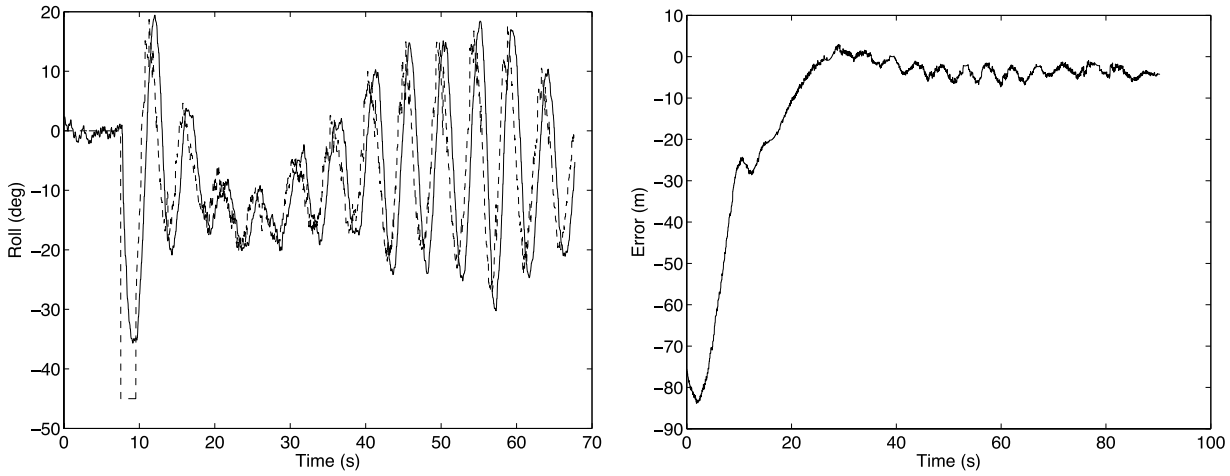

(a) (b)

Fig. 16. (a) Desired versus actual roll angles of the UAV. Dashed line shows the desired path, and solid line shows the actual path. (b) Path error of the UAV during flight.

TABLE IV
PROPERTIES OF THE ORBIT AND CONTROL PARAMETERS USED FOR EXPERIMENTAL TESTS

Parameter	Value
Orbit origin $\mathbf{c}$	$(125, -50, 100)^T\ m$
Orbit direction λ	1
Orbit radius	$125\ m$
Orbit velocity	$15\ m/s$
k_4	0.5
k_5	0.4
$\phi_{\max}$	45°
$\gamma_{\max}$	35°
$\tilde{\psi}_{\max}$	45°
$d_{\min}$	70%

Figs. 15 and 16. The UAV starts inside the radius of $d_{\min}$ and flies straight until it reaches $d_{\min}$ at which point $\phi^c = \phi_{\max}$ until the course angle of the UAV is closer to the desired course angle of the orbit. The UAV then converges onto the orbit.

As shown in Figs. 12(a), 14(a), and 16(a) there are significant oscillations in the commanded roll of the vehicle. In the case of the line, the value of k_2 should be increased to add damping to the lateral response of the UAV. The value of k_5 should be increased to likewise add more damping. The controller can be tuned on the specific platform to remove these oscillations. It is noted here that the controller indeed could have been tuned to perform better. During validation, the responses were not able to be tuned during flight because the only information that was available during flight was the desired and the actual trajectories, which made it difficult to determine that the controller damping was too low.

VI. CONCLUSION

This paper has considered the problem of following straight-lines and orbits in wind using fixed wing unmanned air vehicles where the roll angle and flight path constraints are explicitly considered. The guidance strategies are derived using a kinematic model of the aircraft and using the theory of nested saturations. The resulting strategies are continuous and computationally simple. The contributions of this paper include the following. The guidance laws represented by (13), (20), and (36) explicitly constrain the roll and the flight path angle constraints, and specific conditions on the wind are derived where the guidance laws guarantee asymptotic tracking. In Sections III-A and IV, the nested saturation technique is extended to the problem of path following. This is a nontrivial extension due to the nonlinearities between the integrators. The control strategy for orbit following is complicated by the fact that the nested saturation controller is not guaranteed to converge in a region around the center of the orbit. In Theorem 4.1, we have derived specific conditions for when a simple switching strategy can be used to guaranteed global asymptotic convergence to the orbit. Finally, we have demonstrated the effectiveness of the proposed strategies through simulation and flight tests results.

REFERENCES

[1] P. Aguiar, D. Dačić, J. Hespanha, and P. Kokotović, "Path-following or reference-tracking? An answer relaxing the limits to performance," in *Proc. 5th IFAC/EURON Symp. IAV*, Lisbon, Portugal, Jul. 2004, pp. 1–6.

[2] A. P. Aguiar, J. P. Hespanha, and P. V. Kokotovic, "Path-following for nonminimum phase systems removes performance limitations," *IEEE Trans. Autom. Control*, vol. 50, no. 2, pp. 234–238, Feb. 2005.

[3] J. Hauser and R. Hindman, "Maneuver regulation from trajectory tracking: Feedback linearizable systems," in *Proc. IFAC Symp. Nonlinear Control Syst. Des.*, Tahoe City, CA, USA, Jun. 1995, pp. 595–600.

[4] P. Encarnação and A. Pascoal, "Combined trajectory tracking and path following: An application to the coordinated control of marine craft," in *Proc. 40th IEEE Conf. Decision Control*, Orlando, FL, USA, Dec. 2001, pp. 964–969.

[5] R. Skjetne, T. Fossen, and P. Kokotović, "Robust output maneuvering for a class of nonlinear systems," *Automatica*, vol. 40, no. 3, pp. 373–383, Mar. 2004.
[6] R. Rysdyk, "UAV path following for constant line-of-sight," in *Proc. AIAA 2nd Unmanned Unlimited Conf.*, Sep. 2003, no. AIAA-2003-6626, pp. 1–10.
[7] R. W. Beard and T. W. McLain, *Small Unmanned Aircraft: Theory and Practice*. Princeton, NJ, USA: Princeton Univ. Press, 2012.
[8] D. R. Nelson, D. B. Barber, T. W. McLain, and R. W. Beard, "Vector field path following for miniature air vehicles," *IEEE Trans. Robot.*, vol. 37, no. 3, pp. 519–529, Jun. 2007.
[9] D. R. Nelson, D. B. Barber, T. W. McLain, and R. W. Beard, "Vector field path following for small unmanned air vehicles," in *Proc. Amer. Control Conf.*, Minneapolis, MN, USA, Jun. 2006, pp. 5788–5794.
[10] D. A. Lawrence, E. W. Frew, and W. J. Pisano, "Lyapunov vector fields for autonomous UAV flight control," *AIAA J. Guid., Control, Dyn.*, vol. 31, no. 5, pp. 1220–12229, Sep./Oct. 2008.
[11] E. W. Frew and D. Lawrence, "Tracking expanding star curves using guidance vector fields," in *Proc. Amer. Control Conf.*, Montreal, QC, Canada, Jun. 2012, pp. 1749–1754.
[12] V. M. Goncalves, L. C. A. Pimenta, C. A. Maia, B. C. O. Durtra, and G. A. S. Pereira, "Vector fields for robot navigation along time-varying curves in n-dimensions," *IEEE Trans. Robot.*, vol. 26, no. 4, pp. 647–659, Aug. 2010.
[13] A. Brezoescu, T. Espinoza, P. Castillo, and R. Lozano, "Adaptive trajectory following control of a fixed-wind UAV in presence of crosswind," *J. Intell. Robot. Syst.*, vol. 69, nos. 1–4, pp. 257–271, Jan. 2013.
[14] S. Park, J. Deyst, and J. P. How, "Performance and Lyapunov stability of a nonlinear path-following guidance method," *AIAA J. Guid., Control, Dyn.*, vol. 30, no. 6, pp. 1718–1728, Nov./Dec. 2007.
[15] A. R. Teel, "Global stabilization and restricted tracking for multiple integrators with bounded controls," *Syst. Control Lett.*, vol. 18, no. 3, pp. 165–171, Mar. 1992.
[16] P. Castillo, R. Lozano, and A. E. Dzul, *Modelling and Control of Mini-Flying Machines*. New York, NY, USA: Springer-Verlag, 2005.
[17] P. Castillo, R. Lozano, and A. Dzul, "Stabilization of a mini rotorcraft with four rotors," *IEEE Control Syst. Mag.*, vol. 25, no. 6, pp. 45–55, Dec. 2005.
[18] H. Chitsaz and S. M. LaValle, "Time-optimal paths for a Dubins airplane," in *Proc. 46th IEEE Conf. Decision Control*, Dec. 2007, pp. 2379–2384.
[19] R. W. Beard and J. Humpherys, "Following straight line and orbit paths with input constraints," in *Proc. Amer. Control Conf.*, San Francisco, CA, USA, Jun. 2011, pp. 1587–1592.
[20] H. K. Khalil, *Nonlinear Systems*, 3rd ed. Upper Saddle River, NJ, USA: Prentice-Hall, 2002.

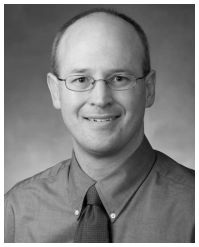

Randal W. Beard received the Ph.D. degree in electrical engineering from Rensselaer Polytechnic Institute, Troy, NY, USA, in 1995.

He has been with the Electrical and Computer Engineering Department, Brigham Young University, Provo, UT, USA, since 1996, where he is currently a Professor. In 1997 and 1998, he was a Summer Faculty Fellow with the Jet Propulsion Laboratory, California Institute of Technology, Pasadena, CA, USA. From 2006 to 2007, he was a National Research Council Fellow with the Air Force Research Laboratories, Eglin Air Force Base, Fort Walton Beach, FL, USA. His current research interests include autonomous systems, unmanned air vehicles, and multiple vehicle coordination and control.

Dr. Beard is a Former Associate Editor for the IEEE TRANSACTIONS ON AUTOMATIC CONTROL, the *Journal of Intelligent and Robotics Systems*, and the IEEE CONTROL SYSTEMS MAGAZINE.

Jeff Ferrin received the M.S. degree in mechanical engineering from Utah State University, Logan, UT, USA, in 2007. He is currently pursuing the Ph.D. degree in mechanical engineering with Brigham Young University, Provo, UT, USA.

He has been with Autonomous Solutions, Logan, since 2007, where he specializes in the control of unmanned ground vehicles. Since 2010, he has been a Graduate Research Assistant with the MAGICC Laboratory, Brigham Young University. His current research interests include vision-based navigation and controls.

Jeffrey Humpherys received the Ph.D. degree in mathematics from Indiana University, IN, USA, in 2002.

He was an Arnold Ross Assistant Professor with The Ohio State University, Columbus, OH, USA, from 2002 to 2005, before joining the faculty of Brigham Young University, Provo, UT, USA, in 2005. He has published papers in operations research, applied probability, finance, and control theory. He has served as a Technical and Scientific Consultant for several companies since 1999, in particular businesses specializing in information technology, financial services, retail, healthcare, and manufacturing. His current research interests include differential equations and numerical analysis.

Dr. Humpherys was a recipient of several grants from the National Science Foundation, including the CAREER Award in 2009.